Initial investigation on different types of clouds observed by Mars Colour Camera (MCC) from India's first Mars Orbiter Mission (MOM)

Jyotirmoy Kalita*, and Anirban Guha
Department of Physics, Tripura University, Suryamaninagar, Tripura-799022, India
*Email: jyotirmoy.physics@tripurauniv.in
Phone: +91-757798089/6009809759

Key point:

- Deep convection plays a major role in the formation of high-altitude clouds.
- Westerlies remarkably contribute to the formation of lee wave clouds.
- CO_2 clouds may reach up to a height of ~40km.
- Morning and evening haze are mainly water ice and carbonic acid in nature.

Abstract:

In the present work, we analysed different types of clouds observed at the limb as well as over the surface of the red planet, captured by MCC onboard the Indian Mars Orbiter Mission during orbit number 44,45,48,49, 50,51,179,187,190,191,466 and 474. The estimated height of the high-altitude cloud (HAC) varies from 40 to 76 km and horizontal spreading of 400 to 1100 km. We used ARC-GIS to detect the area over which the high-altitude clouds are observed. These detached layers of clouds are followed by a haze of dust and water-ice particles. MRO-MCS and MARCI confirm a few dust events during the appearance of the high-altitude cloud. The estimated wavelength of the Lee wave cloud varies from 38 to 44 km while wind speed varies from 54 to 64 m/sec. Aerosol Optical Depth (AOD) as a function of altitude varies from 0.6 to 2.4 for the red channel and 0.8 to 1.8 for the blue channel with an effective radius of 0.2 to 3.0 μm for the aerosol. We consulted the Global Circulation Model (GCM) as well as MOLA-DEM to frame the AOD output. Estimated wind speed profile from MCC and MARCI-MGDM suggested the circulation of strong wind across the globe and delivered input to the formation of clouds through different processes related to the atmosphere dynamics viz. Deep Convection, Orographic lift, Thermal updraft, etc. In our present study, we tried to estimate the parameter related to these processes and tried to correlate them with the observed events.

Plain Language Summary:

Martian water ice and dust cloud always hold the researcher's quest to explore the probable exoplanet habitat. These clouds are also captured by Mars Colour Camera (MCC) during the operational period from 2014 to 2017. In our present study, we considered a total of 60 images (Limb view and Nadir view) from ISRO-MOM data to report the atmospheric characteristics of cloud events captured by MCC. High atmospheric aerosol during dust storm season increases the AOD and prevents solar insolation signifying a high albedo value. As the albedo increases, temperature decreases at the top of the atmosphere (TOA) creating a favourable condition for the formation of clouds. Due to adiabatic cooling during deep convection, the water ice parcel reaches a remarkable height in the mesosphere. Initially, the cloud has been observed through limb view and further we carry out our work to study nadir view clouds usually appears near high land of Mars. The formation temperature of the clouds varies from 180K to 200K. A strong wind shear drives the cloud parcel towards the north-western

direction. The nadir view cloud's starting point follows the trapped lee wave structure, and further, it follows the propagating lee wave pattern.

Introduction:

Orbiting spacecraft are capturing images of clouds over the planet's edge regularly for the last few decades. (Anderson and Leovy, 1978, Santer et al., 1986 and Jaquin et al., 1986). A detached layer has been observed above a continuous but non-uniform haze over the limb geometry at a considerable altitude of 40 to 80 Km from the past Mars missions. (Anderson and Leovy, 1978; Jaquin et al., 1986, Heavens et al., 2015). The continuous haze is formed of water ice particles and dust whereas the detached layer is composed of H_2O ice hexagonal crystals, reported based on the wavelength-dependent vertical reflectivity profiles with maximum reflection values at red wavelengths i.e. I/F ~0.2 (Jaquin et al., 1986; Clancy et al., 2007; Smith et al., 2013). On the other hand, Heavens et al., 2015 reported that dust can be transported at high altitudes up to z ~80 km, called "Extreme Detached Dust Layers" EDDL (Heavens et al., 2015). The formation mechanism of EDDL by vertical transport of dust can be occurring by several processes viz. Dust storms, intense updrafts over volcanoes, Hadley circulation and rocket dust convection (Spiga et al., 2013; Heavens et al., 2015).

Past Mars missions consulted radio occultation, IR radiance scan, imaging of the limb features etc. to detect the high-altitude clouds. (Chassefiere et al., 1992; Clancy et al., 2014; Heavens et al., 2011, 2015; Montmessin et al., 2006, 2007; Määttänen et al., 2010; Määttänen et al., 2013a; Smith et al., 2013). Based on a statistical analysis of aerosol distribution observed by Mars Climate Sounder (MCS) Sefton-Nash et al. (2013) show that the mesospheric clouds can be formed of CO_2 ice, water ice or dust.

A recent study shows another possibility that water-ice clouds can be formed at a height of 80-90 km due to the influence of interplanetary dust particles (Hartwick et al., 2019). Also, in March–April 2012, very high-altitude plumes in the Martian limb reaching peak altitudes of z ~200–250 km was reported (Sánchez-Lavega et al., 2015). In order to acquire more knowledge by going deep into the high-altitude cloud events, we designed our present work based on the cloud images captured by MCC onboard Mangalyaan. We consulted the MCD model (Forget et al., 1999) to compare our results and to report how the deep convective activity leads to the lifting of the dust particle during the dust storm season.

Standing-wave patterns of the cloud near-surface features of high relief were captured by Mariner-9 (Wildey et al., 1974). These standing waves or Lee-wave clouds are observed in a stable atmosphere associated with surface obstacles like mountains or coasts are responsible for the generation of Lee-wave clouds (Ray et al., 1986, Kahn et al., 1984). Wind passing over such features receives a vertical pulse, and thus, the kinetic energy is transformed into potential energy (Durran et al., 1990). Our present work is dealing with the trapped Lee-wave clouds. Air rises to the colder region in the crest of the wave, and hence, condensation occurs due to the adiabatic cooling to form the elongated over the surface of high relief (Ray et al., 1986). These elongated condensate clouds with high wind speed are aligned orthogonally to the prevailing wind direction if the obstacle is a Mons range (Wood et al., 2003, Kahn et al., 1984). The formation of the water–ice cloud and dust particles' participation causes a high haze over the Acidalia Region (Benson et al., 2006).

Our present works estimated the properties of the cloud haze and validated our initial results with the global circulation model (GCM) model based on the Mars Climate Database (MCD) http://www-mars.lmd.jussieu.fr/mcd_python/. We used MOLA-DEM (MGS) data to estimate the elevation of different surface features. For that, we processed the MOLA map in ARC-GIS software to extract the surface elevation data. We also estimated other parameters like temperature, Albedo, and AOD for the observed region using ISRO-MOM data processed in the MATLAB platform.

3. Theoretical background and methodology:

3.1 MCC data analysis:

The present work considered the MCC images as primary data. We consulted GIMP and MATLAB to enhance the contrast and pre-analysis processing of the MCC images. Since the spatial resolution value varies from pixel to pixel in the image plane, we perform angle and lens correction before including the images for scientific observation.

3.1.1 Extracting the cloud location:

In the mentioned methodology, we locate the position of the cloud by projecting MCC raster images over the MOLA-DEM using ARC-GIS software. MCC image raster data is available with the MCC-AREO image data file.

3.1.2 Extracting Reflectance value:

We converted the image DN values to radiance, planetary reflectance and further radiance to reflectance at TOA as follows,

$$Radiance_{\lambda} = \frac{Radiance_{\max_{\lambda}} - Radiance_{\min_{\lambda}}}{QCAL_{\max_{\lambda}} - QCAL_{\min_{\lambda}}} * (QCAL - QCAL_{\min}) + Radiance_{\min_{\lambda}} \quad (1)$$

$$\rho_{\lambda} = \pi * Radiance_{\lambda} * \frac{d^2}{ESUN_{\lambda}} * \cos\theta \quad (2)$$

The MCC visible bands radiance data (λ) can be converted to top of atmosphere reflectance (I/Fλ) using the observation constraints and a solar spectrum scaled to Mars–Sun distance. The (I/Fλ) is defined as,

$$\frac{I}{F_{\lambda}} = \frac{\pi L_{\lambda}}{F_{(\lambda,0)} \cos i \cos\theta} \quad (3)$$

Where L_{λ} , i, and θ_0 refer to the spectral radiance observed by MCC, the apparatus incidence angle, and the solar zenith angle, respectively. QCALMIN = the minimum quantized calibrated pixel value (typically = 1) QCALMAX = the maximum quantized calibrated pixel value (typically = 255). F_{λ} refers to Mars-Sun distance corrected top of the atmosphere incoming solar flux per unit of surface (Mishra et al., 2016).

3.1.3 Pixel value correction:

The limb of the red planet in the reflectance curve is fixed as follows,

$$height\ of\ the\ cloud = N_{sc}R_{spatial} + error \quad (4)$$

N_{SC} is the number of pixels counted from the surface to the cloud. $R_{Spatial}$ is the spatial pixel resolution at the centre of the image and the probable error related to the correction mentioned above

After the angle correction, spatial pixel resolution (m, n) at any given coordinate (i, j) can be expressed as,

$$(m,n) = \left(\frac{a}{2},\frac{b}{2}\right) * \left(\frac{1}{\cos(observer\_zenith\_at\_(i,j))}\right) \quad (5)$$

The next algorithm is based on the Pythagoras theorem to correct the pixel values and calculate the cloud's height as follows,

$$d_{limb} = \sqrt{r^2 - R_{planet}^2} \quad (6)$$

$$spatial\ pixel\ resolution_{limb} = resolution\ constant.d_{limb} \quad (7)$$

Further, we consider the separate layer to be homogeneously spread over the complete disc and estimate the height of the cloud.

3.1.4 Wavelength and Wind speed Calculation:

According to the relevant literature, the wavelength of the lee wave cloud is given by (**Singh et al., 2018**),

$$LW(\lambda) = 2\pi u c_s / g\sqrt{\gamma - 1 - \gamma^2 * u^2 / 4c^2} \quad (8)$$

We may rearrange the equation as follows (**Portyankina et al., 2005**),

$$u = gLW(\lambda)\sqrt{(\gamma - 1)} / 2\pi c_s \quad (9)$$

Where u = wind speed, g= acceleration due to gravity on Mars (3.69 m/s2), LW (λ) = wavelength, γ=Cp/Cv (1.3055), and cs=sound speed for mars~ (226 m/s). Utilizing equation 2.2.1, we estimate the horizontal wind speed that drives the cloud parcel along the northeastern slope of the high ridge topography of Mars. The speed of light is very high compared to the wind's speed, and hence (such that u2/c2 ≈ 10−3) the third term inside the square root will vanish. (**Mishra et al., 2016; Kalita et al., 2021 (a & b)**)

In our present work, estimated wind speed is slightly higher for the Martian atmosphere according to previous wind speed estimates and model results (**Mischna et al., 1998; Murphy et al., 1990; Forget et al., 1999**).

3.1.5 Stereo Image method to calculate AOD:

In this particular process, the radiation at the top of the atmosphere as observed by the camera onboard an Orbiter is given by,

$$O(i,j) = R(i,j)\exp(-\tau/\mu_2) + B(i,j) \quad (10)$$

Since B will not show considerable variation over an observed area hence, we may convert the above equation as,

$$contrast(O_1) = (contrast(R_1(i,j)\exp(-\tau/\mu_1) \quad (11)$$

$$contrast(O_2) = (contrast(R_2(i,j)\exp(-\tau/\mu_2) \quad (12)$$

For a Lambertian surface, R_1=R_2 for a perfect camera. Therefore, if we use Lambertian approximation in Eq. 5, we have,

$$contrast(O_1) = \exp(-\tau/\mu_1)(contrast(R_1)\} \quad (13)$$

$$contrast(O_2) = \exp(-\tau/\mu_2)(contrast(R_2)\} \quad (14)$$

Now, the expression of AOD can be written as,

$$\tau = [\mu_1\mu_2/\mu_1 - \mu_2]\log\{(contrast(O_1)/<O_1>)/(contrast(O_2)/<O_2>)\} \quad (15)$$

Thus, we may estimate the AOD from two stereo images captured by a camera. (**Mishra et al., 2015; Kalita et al., 2021 (a & c)**)

3.1.6 Temperature calculation:

We know that the Stefan–Boltzmann law can be formulated mathematically as follows,

$$L = (\sigma/\pi) * T^4$$
$$=> P = \sigma A T^4 \quad (16)$$

Based on previous literature, we estimated albedo value from the MCC images, and that we used in the modified S-B law and hence we may find the temperature as, (**Leo Presto et al., 2019**),

$$=> T = (1-a)^{1/4}\frac{279}{r^{1/2}}K \quad (17)$$

Where L is the radiance value, σ is Stephen's constant = 5.670367(13) ×10−8 W·m−2·K−4, Where 'T' is the temperature, 'a' denotes albedo value, r is the distance between mars and sun in the atmospheric unit.

3.1.7 Albedo Calculation:

For visible wave-length, we calculated the albedo value as,

Albedo=F+/F-. (18)

3.2 MCS data retrieval:

3.2.1 Opacity data analysis:

MCS observed Martian limb, nadir, and off-nadir in nine broadband channels to detect dust, temperature, and condensates (**McCleese et al., 2007; Kleinböhl et al., 2009**) since September 24, 2006 (LS = 111°, MY 28). We may extract vertical profiles of temperature (K) and water ice extinction (km-1; at 843 cm-1 wavenumbers) through the limb observations with a moderate (5 km) vertical resolution from the surface to ~80 km altitude through MCS observation (**Kleinböhl et al., 2009**). The uncertainty in extinction usually varies from 10−3 and 10−4 km−1 for MCS dust observational data (**Benson et al., 2010**), whereas the uncertainty in the altitude data varies as ±1 km (**Kleinböhl et al., 2009**).

3.2.2 Calculation of effective radius:

We found an error of ~5% from previous literature in calculating effective radius. Also, in GCM, the mixing ratio in mol/mol, which we convert to PPM, found the effective radius within 6.2% error.

$$mixing\ ratio(q_d) = \frac{4\rho_d(\ d_z\tau\ )\ r_{eff}}{3Q_{ext}\rho} \quad (19)$$

Also, the effective radius of water ice particle as,

$$mixing\ ratio(q_I) = \frac{4\rho_I(\ d_z\tau\ )\ r_{eff}}{3Q_{ext}\rho} \quad (20)$$

The value of *'Qext'* is 0.775, which can be obtained from the Mie theory described by (Kleinböhl et al., 2009) *'reff'* is the effective radius of a dust particle, and density is obtained from MCS data using ideal gas equation. 'ρI' is the retrieved density that has the value of 900 kg m-3. The effective radius of the dust particle varies from 1.40 to 3.2 μm. The mixing ratio is considered from the MCD GCM for that particular event. We verified our calculated effective radius with the MCD GCM output for that particular event.

3.3 MARCI and MCD-GCM data retrieval:

We processed the .mov file for the MARCI images to get the image frames where Arsia Mons is visible with the daily water ice cloud's appearance. We used the image frame only to visualize the AMEC event. The weather reports are available at the following link.

http://www.msss.com/msss_images/latest_weather.html. We used the MCD-GCM web interface to extract the wind data. We extracted the S-N and E-W wind values for the required altitude level from the surface for all locations. MCD web interface data is available at http://www-mars.lmd.jussieu.fr/mcd_python/

Results and Discussion:

In the present work, we focused on the three different features captured by Mars Colour Camera (MCC) onboard India's first mission to Mars. We segregated the complete results into three parts. The first section comes up with the results regarding high altitude clouds. In figure 1 we have shown high altitude cloud appears over the edge of the planet.

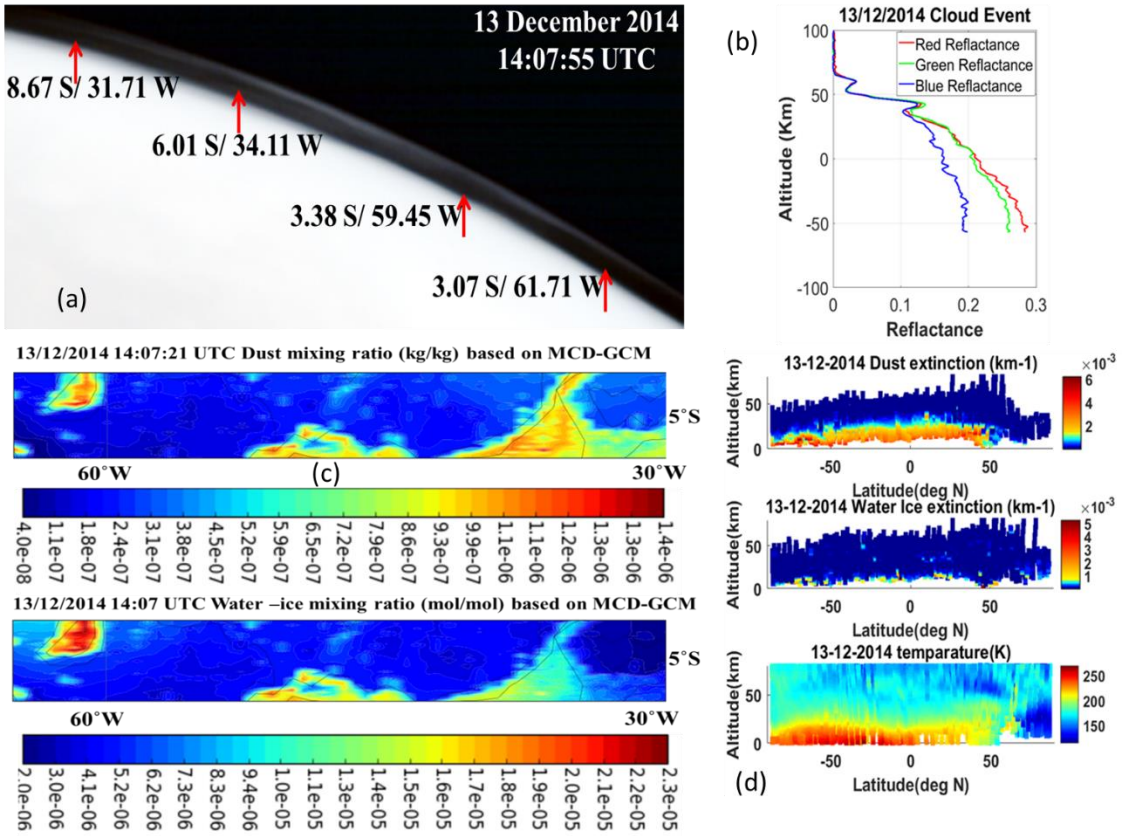

Figure 1: The figure illustrates the analysed result related to high altitude clouds. For the demonstration, we picked the event of 13 December 2014. (a) shows the high-altitude cloud at the edge of the red planet with the location over which it forms. (b) shows the reflectance plot for the high-altitude cloud where we may see the cloud height along with the aerosol haze followed by the detached layer. (c) confirms the presence of dust and water-ice particles over the observed location. For that, we consulted Global Circulation Model based on Mars Climate Database (MCD). (d) shows the real-time observation of dust and water ice extinction along with the temperature profile regarding the observed event.

The present work highlights the analysed result on high altitude clouds appears at the edge of the planet during northern hemisphere summer. High surface temperature, estimated from MCS data, indicates the deep convection activity that helps the air parcel move to a remarkable height of ~40 ± 3

to 90 ± 5 km. Strong westerlies plays a significant role in the cloud's shape, viz. even, uneven structure and drive the air parcel parallel to the limb of the red planet to an extant of ~400 ± 11 to 1200 ± 21 km. A few local, regional, and cross-equatorial dust storms during the observed event that concertize our assumption regarding the reason behind the formation of high-altitude clouds is reported by MARCI daily weather report and images. Estimated reflectance value indicates the presence of water-ice clouds, and the detached layers followed by a continuous haze containing both coarse and fine mode particles. Maximum reflectance in blue channel indicates the water ice and maximum reflectance in red channel indicates the present of dust particle. The present work also estimates the effective radius of the particles present in the detached layer and continuous haze. Estimated effective radius for the water ice particle varies from 0.3 to 3.0 μm and 0.2 to 0.6 μm for the dust particle. Eventually, we reported a CO2 cloud event on December 13, 2014, which needs a deep investigation further to know about the CO2 cloud formation.

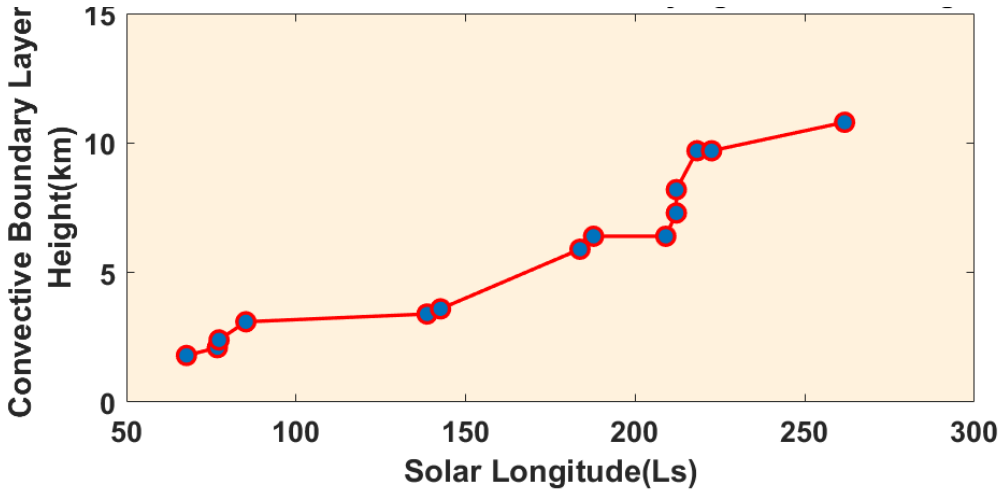

Figure 2: Variation of CBL height with the solar longitude. Above plot firmly helped to estimate the vertical mixing of air from the curve. Blue circle represents the exact CBL data point at different observed solar longitude (Ls).

After the dust storm, high deposition of dust prevents the solar radiation and contributes to the cooling process of the surface. As a result, the deep convection reduces, and the air parcel could move to 40–

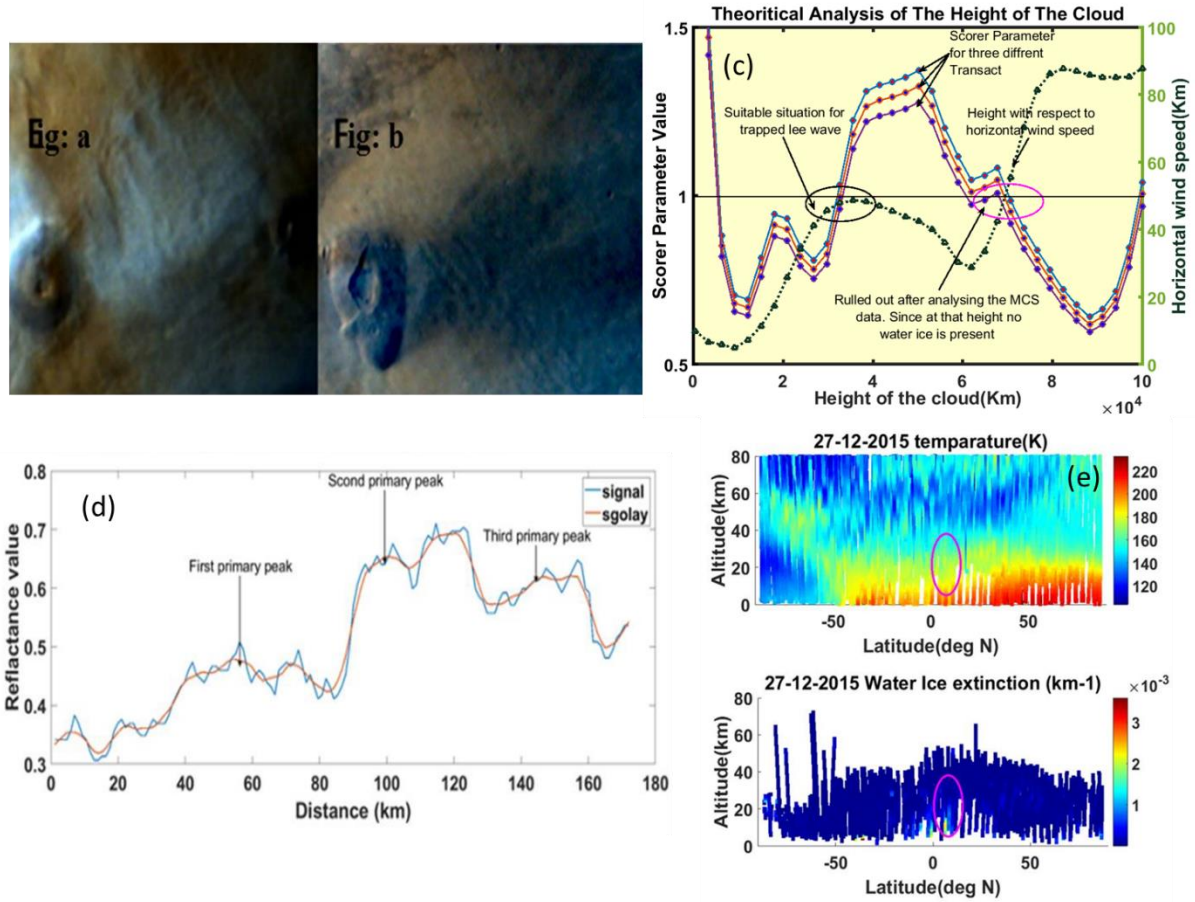

50 km due to the warm temperature maintain by the dust coverage. During the pre-dust storm season, deep convection process is more impactful, and contributes in the formation of the high-altitude water ice cloud. Spatio temporal variation of AOD and CBL reveals the hidden reason for high altitude water ice clouds. Figure 2 shows the variation of CBL during observed period in terms of solar longitude. Reported scale height suggested a homogeneous mixture of air and air-born dust over the observed area. We need more specific data to report the complete process involved in the formation of the high-altitude cloud. From figure 2 we may see that during non-dust storm season CBL heigh is only 5-6 km suggested the weak mixing of air and aerosol. Due to which we may see thick cloud over the lee side of the Martian Volcanos. On the other hand, during dust storm season the plot suggest an increment in the height of CBL and strong mixing. As a result, we may observe thin layer over a continues haze or high-altitude cloud.

Figure 3: The figure illustrates the analysed result related to the lee wave cloud observed in the Martian atmosphere. (a) & (b) show the formation of the lee wave cloud near Ascraeus mons and Thersis tholus.
(c) shows the scorer parameter relation with heigh and vertical wind from which we may estimate the height of the cloud. (d) shows the blue reflectance value along the slope of the Mons and Crater from which we may estimate the wavelength of the cloud. (e) illustrate the analysed MCS data to verify the calculated height through water ice extinction. MCS also confirms the formation temperature for the lee wave cloud which we have estimated through albedo value.

The second section comes up with the result regarding the lee wave clouds observed over Martian high land, mons and well-known Martian Volcanos. The present work estimated various parameters associated with the formation of the Lee-wave cloud and tried to interpret the results with different supporting datasets and model. We used the Lee-wave cloud images captured by MCC for the present work and estimated different atmospheric parameters like wind speed, optical depth, albedo value, temperature, etc. In the present study, the estimated wavelength of the Lee-wave cloud varies from 25 ± 2 to 33 ± 2 km, whereas wind speed ranges from 39 ± 9 to 49 ± 9 m/s. This moderate wind speed helps in the formation of a Lee-wave cloud.

During the observed period, especially during non-dust storm season, strong westerly can raise the cloud to a higher altitude in the troposphere or sometimes to the mesosphere. The present work estimated Scorer parameter values to report the type of cloud. The estimated scorer parameter value varies from 0.5 to 1.0 suggested the formation of a trapped Lee-wave cloud over the lee side of the Martian Volcao. Since it is a trapped lee wave, hence figure 3 demonstrate the hypothetical height of the cloud using. The estimated cloud height varies from 25 ± 3 to 33 ± 3 km. We may conclude that strong westerlies can raise the cloud to a height of 36 km. The Amstrong exponent varies from 0.6 to 1.2 suggested that the Lee-wave cloud contains both coarse mode and fine-mode particles with an effective radius varies from 0.3 to 3.0 μm. The estimated AOD value varies from 0.5 to 1.8 for the red channel, and the blue channel is at a level of 0.9 to 2.3. Thus, it provided us the information about the distribution of the aerosols for the observed period. We plotted the AOD against the height to estimate the scale height of the AOD. Depending on the exponential fit, the scale height of AOD varies from 3 to 5 km. At the same time, pressure scale height varies from 9 to 11 km. We find a mismatch between the scale height of AOD and the pressure scale height, which suggests the presence of a heterogeneous mixture of air and airborne dust near the observed area. We also estimated the albedo values depending on the radiance value extracted from the MCC image. It varies from 0.7 to 0.9 for the cloudy region. Estimated AOD values confirm the clouds are purely water–ice clouds. We also calculated the temperature using the albedo values and compare the values with GCM yielding a 2.7% error in the calculation. The estimated temperature for the Lee-wave cloud varies from 160 ± 3 to 180 ± 4 K. In Fig. 3, we may see a wave-like pattern near another crater Tharsis Tholus. We also studied the gravity wave cloud and bright haze near Tharsis Tholus. We have estimated the atmospheric parameters for the bright haze as well as for the wave cloud. Far from the crater region, we found a homogeneous mixture of air and airborne dust, which is satisfied by the previous literature and indicates haze near Tharsis Tholus. Near to the crater region, the mixture is not homogeneous, where we may observe Lee wave clouds.

The third section comes up with the observation of morning and evening haze near Martian Land and Martian Craters. Figure 3(b) shows the appearance of have near the Martian Crater. We followed the same analysis and found that the haze is mostly water ice and CO2. We performed reflectance analysis and found maximum reflectance in blue and green channel. It is to be mention that preliminary observation may not enough to report this seasonal haze in a more rigid manner. So we need further investigation on these morning and evening haze.

Conclusion:

1. The northern summer Martian high altitude cloud during Martian year 32 has been investigated in the present work. Aerosol deposition and high surface temperature result in deep convection activity during Martin northern summer which further helps the air parcel move to a remarkable height of ~46±3 to 93±5 km. The Seasonal Strong Westerlies (SSW) drive the air parcel parallel to the limb and redistributed the aerosol up to an extent of

~400±11 to 1200±21 km along the limb. The SSW plays a significant role in the cloud's shape, viz. even, uneven structure. MARCI-DGM reported a few local, regional, and cross-equatorial dust storms during the observed event and visualized through weekly videos, that concertize our assumption regarding the reason behind the formation of high-altitude clouds.

2. The reported reflectance value indicates the presence of water-ice in the cloud stake followed by a continuous haze containing both coarse and fine mode particles. The present work also reported a CO_2 cloud event on 13/12/2014. The CO_2 cloud is observed at the limb of the planet and has been verified through the reflectance analyse.
3. The Post dust storm period accompanies the high deposition of dust, contributes to the cooling process of the surface; hence deep convection reduces, and the air parcel could move to 40 to 50 km. The pre-dust storm season accompanies deep convection process in a more sustainable way, leading to the formation of Martian high-altitude water ice cloud.
4. Spatial variation of AOD and CBL addressed the hidden reason for the formation of high-altitude water ice clouds. Reported scale height of AOD suggested a homogeneous mixture of air and air-born dust over the observed area. The same has been supported by the increment in CBL height indicates the strong mixing of aerosol through the boundary layer.
5. In the present study, estimated wavelength of the lee-wave cloud varies from 25±2 to 33±2 km, whereas wind speed ranges from 39±9 m/s to 49±9m/s. This moderate wind speed helps in the formation of a lee-wave cloud. During the observed period, strong westerly wind can raise the cloud to a higher altitude in the troposphere. Scorer parameter (SP) value varies from 0.5 to 1.0 suggested that it is a trapped lee-wave cloud. SP plot estimated the height of the cloud varies from 25±3 to 33±3 Km.
6. We found that the lee-wave cloud contains both coarse modes as well as fine mode particles. We estimated the mode of the particle depends on the values of Angstrom Exponent (α). The estimated AOD value varies from 0.5 to 1.8 for the red channel, and the blue channel is at a level of 0.9 to 2.3. The mismatch between the scale height of AOD and the pressure scale height, suggests the presence of a heterogeneous mixture of air and airborne dust near the observed area. The same has been supported by the reduction in CBL height indicates weak mixing over the observed area.
7. The present study consulted and accordingly analysed the MCS extinction data for dust and water ice. Using Mixing ratio, we find the size of the dust particle varies from 0.2 to 1.2 μm and for water ice it varies from 0.3 to 3.0μm.
8. Albedo values varies from 0.7 to 0.9 for the cloudy region. We also calculated the temperature using the albedo values and compare the values with GCM yields a 2.7% error in the calculation. The estimated temperature for the lee-wave cloud varies from 160±3 K to 180±4 K.
9. The present work also analyzed the characteristics of the largest lee wave structure associated with AMEC and basically it is a form of offseason lee wave cloud. Except wind speed and spreading distance, AMEC used to follow other parameter same as seasonal lee wave cloud. Wind speed for AMEC sometimes reaches ~96 m/s and due to the high wind speed the spreading distance become 400 km.

Acknowledgement:

The authors are also thankful for the MCC data product team members for providing access to the required data for the present analysis (https://mrbrowse.issdc.gov.in/MOMLTA/) and the Indian Space Research Organization (ISRO) for funding the project with fund reference ISRO/SSPO/MOM-

AO/2016-2019. A special thanks to Dr. Satadru Bhattacharya, Planetary Sciences Division, and Space Applications Centre (ISRO) for his constant support. An acknowledgment is due to the Department of Science and Technology for a supporting fund to the Department of Physics, Tripura University through DST-FIST fund reference SR/FST/PSI-191/2014.

References:

1. Anderson, E., & Leovy, C. (1978). Mariner 9 Television Limb Observations of Dust and Ice Hazes on Mars. Journal of the Atmospheric Sciences, 35(4), 723–734. https://doi.org/10.1175/1520-0469(1978)035<0723:MTLOOD>2.0.CO;2
2. Jaquin, F., Gierasch, P., & Kahn, R. (1986). The vertical structure of limb hazes in the Martian atmosphere. Icarus, 68(3), 442–461.
3. Santer, R. & Deschamps, M. & Ksanfomality, L. & Dollfus, A.. (1986). Photopolarimetry of Martian Aerosols: II. Limb and Terminator Measurements. Astronomy and Astrophysics. 158. 247-258.
4. Smith, M.D., 2002. The annual cycle of water vapor on Mars as observed by the thermal emission spectrometer. J. Geophys. Res. 107, 5115, https://doi.org/10.1029/2001JE001522.
5. Heavens, N. G., Kass, D. M., Shirley, J. H., Piqueux, S., & Cantor, B. A. (2019). An Observational Overview of Dusty Deep Convection in Martian Dust Storms. Journal of the Atmospheric Sciences. https://doi.org/10.1175/JAS-D-19-0042.1
6. Clancy, R., Montmessin, F., Benson, J., Daerden, F., Colaprete, A., & Wolff, M. (2017). The Atmosphere and Climate of Mars (Cambridge planetary science (pp. 76–105). Cambridge: CambridgeUniversityPress. https://doi.org/10.1017/9781139060172.005i:10.1016/j.icarus.2019.05.041
7. Markiewicz, W. J., Sablotny, R. M., Keller, H. U., Thomas, N., Titov, D., & Smith, P. H. (1999). Optical properties of the Martian aerosols as derived from Imager for Mars Pathfinder midday sky brightness data. Journal of Geophysical Research: Planets, 104(E4), 9009–9017. https://doi.org/10.1029/1998je900033
8. McCleese, D. J., (2007). Mars Climate Sounder: An investigation of thermal and water vapor structure, dust and condensate distributions in the atmosphere, and energy balance of the polar regions, J. Geophys. Res., 112, E05S06, https://doi.org/10.1029/2006JE002790
9. Mischna, M., J.F. Bell III, P.B. James., D. Crisp., (1998). Synoptic measurements of Martian winds using the Hubble Space Telescope, Geophys. Res. Lett., 25, 611-614, https://doi.org/10.1029/98GL50358
10. Benson, J. L., D. M. Kass, A. Kleinböhl, D. J. McCleese, J. T. Schofield, and F. W. Taylor (2010). Mars‟ south polar hood as observed by the Mars Climate Sounder. J. Geophys.Res., https://doi.org/10.1029/2009JE003554
11. Curran, R. J., Conrath, B. J., Hanel, R. A., Kunde, V. G., & Pearl, J. C. (1973). Mars: Mariner 9 Spectroscopic Evidence for H2O Ice Clouds. Science, 182(4110), 381–383. DOI: https://doi.org/10.1126/science.182.4110.381

12. Durran, D. R. (1986). Mountain waves. In Mesoscale Meteorology and Forecasting (P. S. Ray, Ed.), pp. 472–492. Am. Meteorol. Soc.
13. Forget, F., Hourdin, F., Fournier, R., Hourdin, C., Talagrand, O., Collins, M., Huot, J.-P. (1999). Improved general circulation models of the Martian atmosphere from the surface to above 80 km. Journal of Geophysical Research: Planets, 104(E10), 24155–24175. https://doi.org/10.1029/1999je001025
14. G V Portyankina Dissertation Gottingen (2005)
Hernández Bernal, Jorge & Sánchez-Lavega, A. & Río-Gaztelurrutia, T. & Ravanis, Eleni & Cardesin-Moinelo, Alejandro & Connour, K. & Tirsch, Daniela & Ordóñez Etxeberria, Iñaki & Gondet, B. & Wood, S. & Titov, D. & Schneider, N. & Hueso, R. & Jaumann, R. & Hauber, E.. (2020). An Extremely Elongated Cloud over Arsia Mons Volcano on Mars: I. Life Cycle. Journal of Geophysical Research: Planets. 126. https://doi.org/10.1029/2020JE006517
15. Herschel, W. (1784). On the remarkable appearance of the polar regions of the planet Mars, the inclination of its axis, the position of its poles, and its spheroidal figure; with a few hints relating to its real diameter and its atmosphere. Philosophical Transactions of the Royal Society of London, 24, 233–273.
16. Hoekzema, N. M., Garcia-Comas, M., Stenzel, O. J., Grieger, B., Markiewicz, W. J., Gwinner, K., & Keller, H. U. (2010). Optical depth and its scale-height in Valles Marineris from HRSC stereo images. Earth and Planetary Science Letters, 294(3-4), 534–540. https://doi.org/10.1016/j.epsl.2010.02.009
17. Hoekzema, N. M., Garcia-Comas, M., Stenzel, O. J., Petrova, E. V., Thomas, N., Markiewicz, W. J., Delamere, W. A. (2011). Retrieving optical depth from shadows in orbiter images of Mars. Icarus, 214(2), 447–461. https://doi.org/10.1016/j.icarus.2011.06.009
18. Hoekzema, N.M., Garcia Comas, M., Gwinner, K., Grieger, B., Markiewicz, W.J., Keller, H.U., (2007). The Scale-Height of Dust Around Pavonis Mons from HRSC Stereo Images. Seventh International Conference on Mars, LPI Contributions No. 1353, p. 3154.
https://www.mps.mpg.de/phd/theses/atmosphere-surface-vapor-exchange-and-ices-in-the-martian-polar-regions.pdf
19. Kalita, J., Mishra, M.K. & Guha, A. (2021). Martian Lee-wave cloud near Ascraeus Mons during Martian years 33 and 34: a study based on the Mars color camera (MCC) images. Indian J Phys. https://doi.org/10.1007/s12648-020-01978-y
20. Kalita, J., Mishra, M.K. & Guha, A. (2021), Martian limb-viewing clouds: A study based on MCC, MCS and MARCI observations, Planetary and Space Science, Volume 208, 2021, 105347, ISSN 0032-0633, https://doi.org/10.1016/j.pss.2021.105347
21. Kalita, J., & Guha, A. (2021, Off-season lee wave cloud over the Arsia Mons in Mars: A study based on Mars Colour Camera (MCC), Journal of Atmospheric and Solar-Terrestrial Physics, Volume 227, 2022, 105805, ISSN 1364-6826,
https://doi.org/10.1016/j.jastp.2021.105805
22. Strausberg, M. J., H. Wang, M. I. Richardson, S. Ewald, A. D. Toigo, 2005. Observations of the initiation and evolution of the 2001 Mars global dust storm. J. Geophys. Res., 110 (E2).
23. Wang, H., 2007. Dust storms originating in the northern hemisphere during the third mapping year of Mars Global Surveyor. Icarus, 189, 325–343, doi:10.1016/j.icarus.2007.01.014.
24. Wang, H., M. I. Richardson, R. J. Wilson, A. P. Ingersoll, and R. W. Zurek, 2003. Cyclones, Tides, and the Origin of Major Dust Storms on Mars. Geophys. Res. Lett., 30, 9, 1488. Doi:10.1029/2002GL016828.

25. Wang, J.-S., & Nielsen, E. (2003). Behavior of the Martian dayside electron density peak during global dust storms. Planetary and Space Science, 51(4-5), 329–338. https://doi.org/10.1016/S0032-0633(03)00015-1
26. Williams, R. M., Phillips, R. J., & Malin, M. C. (2000). Flow rates and duration within Kasei Valles, Mars: Implications for the formation of a Martian Ocean. Geophysical Research Letters, 27(7), 1073–1076. doi:10.1029/1999gl010957
27. Melnik, O., & Parrot, M. (1998). Electrostatic discharge in Martian dust storms. Journal of Geophysical Research, 103(A12), 29,107–29,117. https://doi.org/10.1029/98JA01954
28. Mishra, M. K., P. Chauhan, R. Singh, S. M. Moorthi, and S. S. Sarkar, 2016. Estimation of dust variability and scale height of Atmospheric Optical Depth (AOD) in the Valles Marineris on Mars by Indian Mars Orbiter Mission (MOM) data. Icarus, 265, 84-94.
29. Rafkin, S. C. R., 2009. A positive radiative-dynamic feedback mechanism for the maintenance and growth of Martian dust storms. J. Geophys. Res., 114, E01009, doi:10.1029/2008JE003217.